



Direct measurement of the muonic content of extensive air showers between 2×10^{17} and 2×10^{18} eV at the Pierre Auger Observatory

The Pierre Auger Collaboration*

The Pierre Auger Observatory, Av. San Martín Norte 306, 5613 Malargüe, Mendoza, Argentina; <http://www.auger.org>

Received: 13 February 2020 / Accepted: 18 May 2020
© The Author(s) 2020

Abstract The hybrid design of the Pierre Auger Observatory allows for the measurement of the properties of extensive air showers initiated by ultra-high energy cosmic rays with unprecedented precision. By using an array of prototype underground muon detectors, we have performed the first direct measurement, by the Auger Collaboration, of the muon content of air showers between 2×10^{17} and 2×10^{18} eV. We have studied the energy evolution of the attenuation-corrected muon density, and compared it to predictions from air shower simulations. The observed densities are found to be larger than those predicted by models. We quantify this discrepancy by combining the measurements from the muon detector with those from the Auger fluorescence detector at $10^{17.5}$ eV and 10^{18} eV. We find that, for the models to explain the data, an increase in the muon density of $38\% \pm 4\%$ ($12\% \pm_{18\%}^{21\%}$ for EPOS-LHC, and of 50% ($53\% \pm 4\%$) ($13\% \pm_{20\%}^{23\%}$ for QGSJETII-04, is respectively needed.

1 Introduction

More than a hundred years after the discovery of cosmic rays (CRs), their origin remains unknown. Because of their low intensity, CRs above $\sim 10^{14}$ eV can only be studied through the detection of the showers of particles, known as extensive air showers (EASs), which they create in the atmosphere. The properties of the particles arriving at the top of the atmosphere are therefore measured indirectly by arrays of on-ground based detectors. As the mass composition of CRs at Earth is of fundamental importance to understand their origin, the identification of observable parameters sensitive to the primary mass is essential.

After the first interaction of a primary cosmic ray with the air molecules, a cascade of secondary particles develops in the atmosphere. The depth of maximum multiplicity of secondary particles, X_{\max} , thanks to its linear dependence on the logarithm of the primary mass A [1], is the most prominent observable to gain information on the primary compo-

sition. Experimentally, it is determined through the observation of the longitudinal shower profile, via Cherenkov or fluorescence detectors. Also very relevant for inference on mass composition is the number of muons in showers. Its relevance can be understood on the basis of the framework of the Heitler-Matthews model of a cascade [1], where the number of produced muons scales with energy E and mass number A as $N_{\mu} \propto AE^{\beta}/(A\xi_c)^{\beta}$. The parameter ξ_c is the critical energy at which charged pions are likely to decay into muons rather than interact. In realistic air shower scenarios, ξ_c is within $20 - 30$ GeV while $\beta \approx 0.9$. Experimentally, the number of muons is determined through the measurement of the muon lateral shower profile, performed by means of ground-based arrays of particle detectors.

The interpretation of X_{\max} and of the number of muons, and in general of every EAS observable sensitive to mass, relies on the comparison of their measured values with those predicted by EAS simulations. These resort to hadronic interaction properties at very high energies and in phase-space regions not well covered by accelerator experiments. Currently, the systematic uncertainties in X_{\max} and in muon-number related quantities predicted by these simulations are dominated by the differences between hadronic interaction models and not by detector uncertainties, even after recent updates based on LHC data of parameters governing the interactions [2]. An internally consistent hadronic interaction model should reproduce simultaneously the different facets of the showers captured in every observable sensitive to the primary mass. Therefore, any additional insight in the evolution of composition-sensitive parameters as a function of energy provides new light on the hadronic processes at energies above those which are achievable with current particle accelerators.

The study of the number of muons is particularly interesting as the accuracy of the simulation predictions is challenged by requiring specific modelling of the number of generations of hadronic interactions and of the properties of their final state, such as the multiplicity and the average fraction of electromagnetic energy per interaction carried by neutral

*e-mail: auger_spokespersons@fnal.gov

pions. The measurement of muon-number related quantities has thus been a long-standing effort carried on with ground-based detector arrays (see, e.g., [3–9]). Several hints that the muon number is larger in observations than in simulations have been reported, with higher tensions at the highest energies [10], although the significance of the measurements is difficult to assess due to the uncertainty in the absolute energy calibration of the showers.

The objective of this work is to bring new information on the muon content in showers, and on its evolution as a function of energy between 2×10^{17} and 2×10^{18} eV, by means of a direct measurement of the muon density at the Pierre Auger Observatory [11, 12]. This is the largest facility built to detect CRs at the highest energies. In operation since 2004 to focus primarily on the energy range above 10^{18} eV, it consists of 1600 water-Cherenkov surface detectors (SD), placed in a triangular grid with a spacing of 1500 m covering an area of about 3000 km² (SD-1500) and 24 air-fluorescence telescopes (FD), grouped at four sites overlooking the SD array.

Subsequent to the completion of the array construction in 2008, new detectors have been added to extend the energy range down to $\approx 10^{17}$ eV: a smaller array of area 23.5 km² composed of 61 surface detectors with 750 m spacing (SD-750), and three fluorescence telescopes with a higher elevation of the field of view. Alongside the SD-750 array, underground muon detectors (UMD) were designed to provide a dedicated device to directly measure the muonic component of EASs. An engineering array of prototypes operated until November 2017 to validate and optimize the detector design, and to evaluate its performance (preliminary results were presented in [13–16]).

In this paper, we report the first measurements made at the Pierre Auger Observatory on muon densities in EASs between 2×10^{17} and 2×10^{18} eV. They have been possible thanks to the capability of muon counting of the UMD prototype array, which is described in Sect. 2. The definition of the muon-density estimator, dubbed ρ_{35} , together with the shower-reconstruction procedure to extract it, are the subject of Sect. 3. The evolution of the muon content with energy is then presented in Sect. 4, in perspective with previous measurements at higher energies and with model expectations. Concluding remarks are given in Sect. 5.

2 Muon counting with the UMD

2.1 The engineering array

The engineering array of the underground muon detector (UMD) consists of seven sets of scintillator detectors, each buried 2.3 m deep next to an SD-station in the SD-750, forming a hexagon (see a sketch in Fig. 1). The depth, correspond-

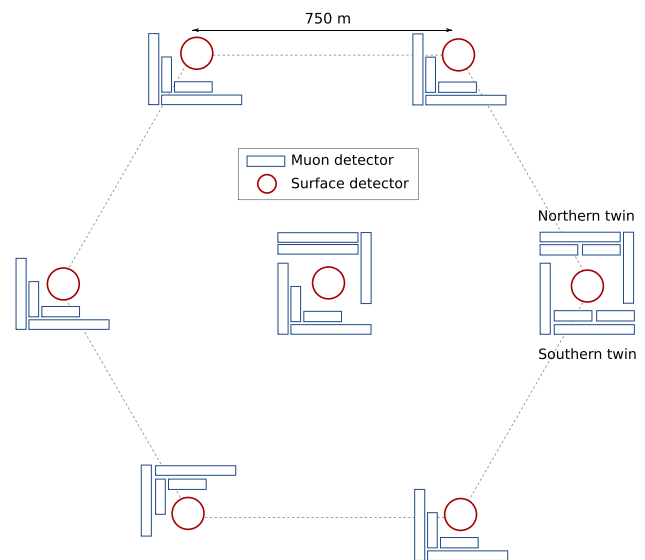


Fig. 1 Sketch of the underground muon detector engineering array. The circles represent the water-Cherenkov detectors. The muon counters are symbolized by the rectangles

ing to ~ 540 g/cm² of overburden as determined by the local soil density, is such that the electromagnetic component of extensive air showers is largely absorbed, while muons with energy in excess of ~ 1 GeV can reach the buried detectors. Each underground detector is installed at least 7 m away from the center of its SD companion, so that shower particles with zenith angles up to 45° can hit the scintillators without passing through the surface detector.

The prototype UMD station is composed of four scintillation modules (SMs), with 2×5 m² and 2×10 m² area. There are two positions equipped with extra stations to assess the detector resolution and its efficiency¹. Each SM consists of 64 plastic scintillation bars sealed in a PVC casing, containing wavelength-shifting optical fibers, a 64 multi-pixel optical device, and acquisition electronics (see [17] for details on the material used and the construction procedures for the scintillation modules). The light produced in the bars is collected and propagated along the fibers which couple to the optical device. Two different types were tested in the engineering array: photo-multiplier tubes (PMTs) and silicon photo-multipliers (SiPMs). For the full array, the SiPM option was chosen because of their better photo-detection efficiency, reduced power consumption, and lower costs [18]. Data used in this work correspond in turn to the one-year period, starting in October 2015, when the engineering array began stable data taking with 64-pixel PMTs, namely the Hamamatsu ultra bi-alkaline H8804-200MOD, a H7546-type PMT but with a different casing and an

¹ For the full UMD array, only three 10 m² will be installed in each position of the SD-750, as the extra station at the centre of the hexagon.

increased quantum efficiency peaking around the wavelength of 350 nm.

The highly segmented UMDs are designed to count individual muons when triggered by the associated SD station. The electronics therefore consists of two components: the underground electronics, installed in each buried SM, and the surface electronics, at the SD station. Both are powered by solar panels. The underground electronics includes the PMT, an analog board to digitize the pulses from the PMTs, a digital board with a field-programmable gate array (FPGA) and memory, as well as a power distribution board and a microcontroller board for data transmission and slow control. The surface electronics, which is common to all UMDs, serves as an interface with the SD electronics to get trigger data and to transfer muon data: it consists of wireless communication to the Central Data Acquisition System (CDAS), the network switch, and the power regulator.

The analog front-end accommodates 64 pre-amplifiers and remotely-adjustable threshold discriminators to convert the analog pulses of each PMT pixel to serial binary signals. Thus, PMT time pulses are converted into a train of digital '0's and '1's corresponding to the absence or presence of a signal above the threshold. The FPGA located on the digital board acquires the data from the analog board with a frequency of 320 MHz, corresponding to a sampling interval of 3.125 ns. In each time bin, one bit per channel is saved in the front-end memory which consists of two circular buffers that can store up to 6.4 μ s of data (2048×3.125 ns). Upon request from the CDAS, the binary traces are recovered and transmitted. The event acquisition is synchronized at the lowest (hardware) level to the surface stations through a dedicated triggering line. The UMD electronics synchronization is achieved through a time-tagging scheme, mostly implemented in the FPGA. An event data trigger request, received by the surface radio, is sent from the surface to the underground microcontroller through an ethernet line. The search of the requested event and the corresponding retrieval of data is also programmed in the FPGA.

2.2 Muon counting methodology

The segmented design of the UMD allows for the identification of muons through simple counting above a given threshold, without the need for a detailed study of the signal structure. However, different sources of background might bias the counting, such as dark-current pulses, cross-talk, after-pulses, and corner-clipping particles. The criterion used to disentangle muons from the background relies on the width of the corresponding signals, since it is much wider for muons than for the background. The consequent methodology adopted for counting the number of muons, described in this section, is rooted in two procedures, one set at the level of the analog data, the other at the digital level. The

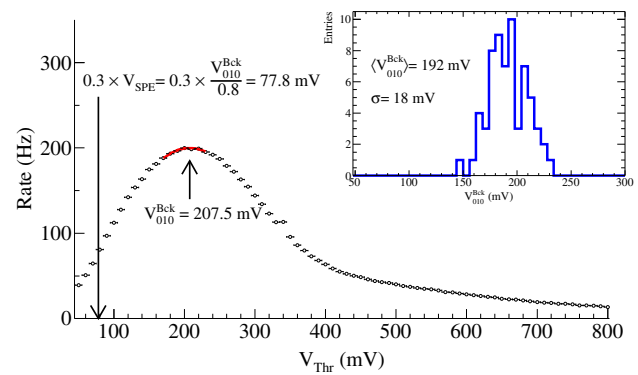


Fig. 2 Background rate, based on a '010' pattern (see text) for an individual scintillator counter as a function of the threshold voltage of the corresponding discriminator channel: in this example the maximum rate is attained for a threshold 207.5 mV. This value, V_{010}^{Bck} , is obtained by fitting the data (red line) and corresponds to 80% of the mean V_{SPE} . The appointed threshold for data acquisition is $0.3 \times V_{SPE}$ is also indicated. The inset histogram shows the distribution of V_{010}^{Bck} for all the 64 discriminator channels sharing the same front-end electronics

former consists in a calibration of the discriminator thresholds applied to analog data, the latter in an algorithm which searches for muon-like patterns in the sequence of the digital data.

2.2.1 Adjustment of the discriminator thresholds

The short background signals, such as those due to cross-talk between adjacent pixels in the PMTs or due to dark/after pulses, are likely to produce analog signals equivalent to a single photoelectron (SPE). The first step to disentangle muons, which generate longer signals, from the background consists in setting the thresholds of the 64 analog-board discriminators so that an SPE is represented by a single '1' or, at maximum, two consecutive '1's in the sampled binary trace. The rationale behind the threshold-adjustment procedure is that, on the one hand, insufficiently high thresholds might produce two or three consecutive '1's. On the other hand, excessively high thresholds would decrease the counting efficiency because the digital output of the discriminator might become too short for the FPGA sampling period. Simulations [19] have shown that the discriminator threshold at the level of 30% of the mean SPE peak amplitude is optimal for the representation of an SPE as a '010' pattern for a sampling period of 3.125 ns.

The threshold calibration is achieved by measuring, for each scintillator channel, the background rate as a function of the discriminator threshold voltage, V_{Thr} , to identify a feature that can be correlated with the mean single photoelectron (SPE) amplitude. The background pulses are composed both of atmospheric muons and self-emitting light in the scintillators. The selected pattern to characterize the background is a single '1' in a time window of 8

bins, i.e., 25 ns, corresponding to a ‘00001000’ pattern and all possible permutations. The rate of such patterns is low for small threshold of discrimination (V_{Thr}) because even narrow signals from baseline noise with small amplitudes will produce more than one ‘1’ in a 8-bin window. The rate is similarly low for high V_{Thr} , because muons with an energy higher than 1 GeV have a low rate. Therefore, the rate of the background patterns is expected to show a maximum: the corresponding value of V_{Thr} , denoted as V_{010}^{Bck} , represents the amplitude of the most probable signal due to the background, i.e., of an SPE. An example of a calibration curve for one individual channel is shown in Fig. 2, where in this case the rate becomes maximal when the threshold voltage is 207.5 mV. The inset of the same figure shows the distribution of V_{010}^{Bck} in all 64 discriminator channels sharing the same front-end electronics. The spread of ~ 18 mV is mainly the result of the typical gain difference among the PMT pixels.

Laboratory measurements² have shown that the mean amplitude of the actual signal due to an SPE, V_{SPE} , can be related to V_{010}^{Bck} by $V_{010}^{\text{Bck}} \approx 0.8 \times V_{\text{SPE}}$. For the period of data taking considered in this paper, the thresholds have been set to $0.3 \times V_{\text{SPE}}$. The calibration routine to build the rate versus voltage curve, as shown in Fig. 2, takes about two hours to be completed. During this procedure, the data acquisition is stopped. Once re-established, the value of the rate R_{010}^{Bck} is continuously monitored and sent every minute to the CDAS for each channel. Every time this monitored rate changes by more than 3σ with respect to its average value, a new calibration procedure is performed.

2.2.2 Muon identification

By applying the threshold calibration described above, the large majority of background events produce a single SPE, the corresponding binary pattern being restricted to one or two consecutive ‘1’s. In contrast, signals due to muons are in general much wider (of the order of 20 ns). They can thus be efficiently identified in the sequence of digital data by a match of the patterns ‘101’ or ‘111’ in three consecutive time bins. This is referred to as 1x1 or gap strategy, as the middle bin x can be either a ‘1’ or a ‘0’, the latter allowing for the possibility of null samples (‘0’) within a binary muon trace. In Fig. 3 the counting procedure is illustrated for a muon pulse as measured in the laboratory: the muon pulse (black line) is discriminated at the level indicated by the horizontal dashed line (V_{Thr}), the discriminator output (dashed blue line) is sampled by the FPGA and, consequently, a digital output is produced.

Muons are then identified by applying a time window, starting from the first identified match ‘1x1’, during which the muon search is inhibited. Without such an inhibition win-

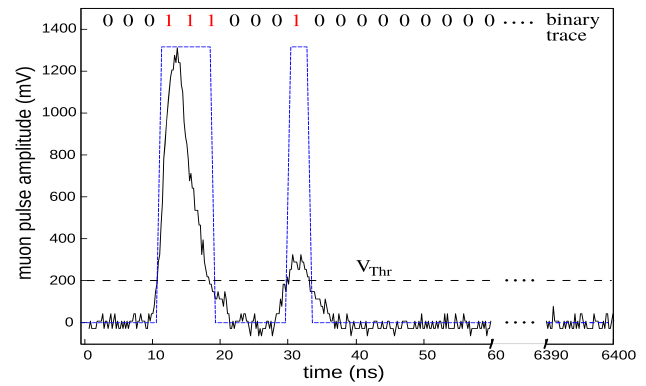


Fig. 3 The counting procedure: a muon pulse (black) is discriminated, and the discriminator signal (dashed blue) is then digitally sampled by an FPGA every 3.125 ns up to 6.4 μ s. As a result, the binary trace on the top of the figure is obtained

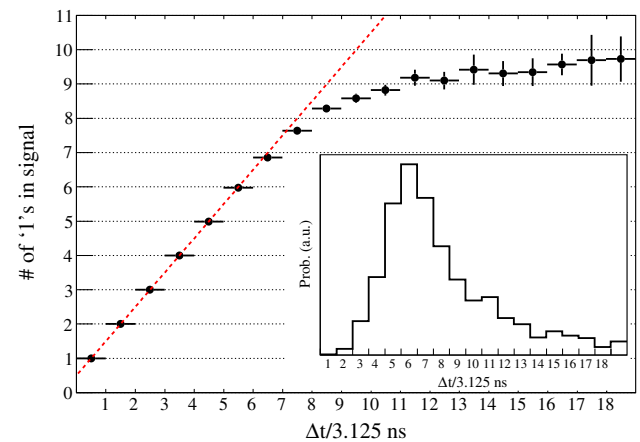


Fig. 4 Relation between the number of ‘1’s and the length of the digital trace, Δt . The red dashed line represents the identity function. The inset shows the distribution of Δt

dow, a single-muon trace including one or more ‘0’s could be interpreted as a sequence of two or more muons. The length of the window has to be long enough to guarantee that most muon traces do not last longer than the window, which would cause an over-counting. In turn, the window duration must not be too long to avoid that multiple muons hitting the same scintillator are not resolved, which would cause an under-counting.

The window length has been determined through the measurement of muons in the laboratory, with the discriminator threshold voltages set at the level of $0.3 \times V_{\text{SPE}}$ and selecting muons crossing the scintillator bar at the edge closest to the PMT. In this position, the width of the signals is maximized, as the light attenuation along the optical fiber is minimal. We show in Fig. 4 the relation between the number of positive samples (‘1’s) and the length of the digital trace, Δt , corresponding to single muons. One can see that the relation is the identity up to signals made of six ‘1’s, i.e., the muon signals are compact (no ‘0’s) up to six ‘1’s. The distribution of Δt

² The setup is described in [18].

in the inset of the same figure shows that the most probable value corresponding to a single muon is six time bins of 3.125 ns. It has to be noted that signals with more than eight '1's depart from the linear behavior, with the number of '1's saturating between nine and ten. These correspond to signals with after-pulses: the saturation implies that the number of '1's generated by these delayed signals, are at most one or two, i.e., consistent with a single SPE.

From the laboratory measurement, the optimal time window was established to be six bins, corresponding to 18.75 ns. However, such a result does not take into account the effects of the time and momentum distribution of muons³ in extensive air showers, which depend not only on the nature and energy of the primary particle, but also on the distance of detection point from the core, neither does it account for the fact that muons can hit the scintillators in different positions with respect to the PMT. To include these effects, we use end-to-end simulations (see section 3.1), from which we find that the optimal time window is seven time bins, i.e., 21.875 ns. This value minimizes the bias for identifying muons even very close to the shower core, where the muon density is high.

The effective efficiency in counting individual muons has also been characterized through the muon measurements in the laboratory. This effect combines both the true detection efficiency of isolated particles with the contamination from long muon signals that produces over-counting. In Fig. 5 it is shown as a function of the time window, for the 5 m² (red points and line) and the 10 m² (black points and line) modules. The shown efficiency is averaged over different impinging positions of the muons on the strips in 0.5 m steps. For the optimal time window of 21.875 ns, it is found to be 104% and 95%, respectively. Values above 100% are due to the over-counting of individual muons as a result of the longer signals in the shorter scintillators where the attenuation of light along the fiber is less important. Furthermore, the efficiency is always smaller for the larger modules because, on average, muons cross the scintillator bars farther with respect to the optical device where the light absorption starts playing an important role.

2.3 Efficiency

At the right-most vertex of the hexagon of the UMD array displayed in Fig. 1, a unique water-Cherenkov detector provides the trigger for two *twin* units with scintillation modules of 30 m², segmented in exactly the same way: 2 × 10 m² plus

³ Note that considering the particle momentum distribution allows correction for the corner-clipping effect happening when muons from a non-vertical direction with respect to the surface of the scintillator deposit their energy in two or more adjacent bars. A detailed explanation of such a correction is given in [20].

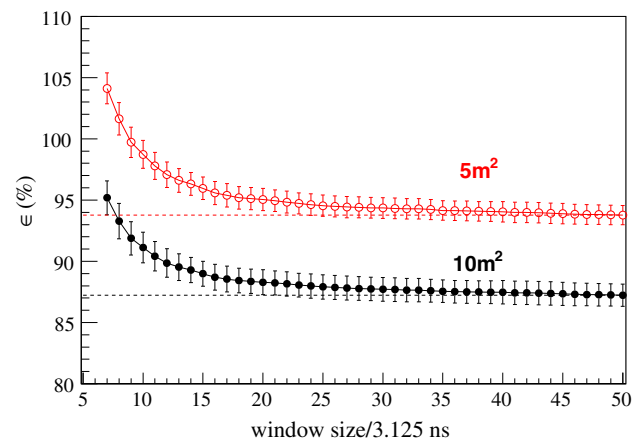


Fig. 5 Efficiency to count individual muons as a function of the time window, for scintillation modules of 10 m² (black points and line) and 5 m² (red points and line)

2 × 5 m². One is deployed towards the south of the surface detector, the other towards the north. These twin units can be used to determine the UMD efficiency.

The average number of muons measured by an ideal counter should depend only on the area of the detector. A counter of an area S should record twice as many particles as a counter with an area $S/2$. In the real case, however, a deviation from this behavior might arise, in particular when there are detection inefficiencies. Therefore, the expected ratio of counts of two detectors with respective areas S_1 and S_2 is

$$r = \epsilon_{\text{rel}} \frac{S_1}{S_2}, \quad (1)$$

where $\epsilon_{\text{rel}} = \epsilon_1/\epsilon_2$ is the relative efficiency between detectors.

The ratio of counts can be estimated in the following way. The probability of measuring N_{1i} and N_{2i} particles simultaneously for a single event i follows from the product of two Poisson distributions with expectation numbers $\mu_i \propto \epsilon_1 S_1$ and $\nu_i \propto \epsilon_2 S_2$. The joint probability distribution can then be explicitly written in terms of the sum $q_i = \mu_i + \nu_i$ and of the i -independent ratio $r = \mu_i/\nu_i$ as

$$\begin{aligned} \mathcal{P}(N_{1i}, N_{2i}|q_i, r) &= \frac{1}{N_{1i}! N_{2i}!} q_i^{N_{1i}+N_{2i}} e^{-q_i} r^{N_{1i}} (1+r)^{-(N_{1i}+N_{2i})}. \end{aligned} \quad (2)$$

The estimator for the ratio, \hat{r} , is found by maximizing the likelihood function of N -events

$$\mathcal{L}(q_1, \dots, q_N, r) = \prod_{i=1}^N \mathcal{P}(N_{1i}, N_{2i}|q_i, r), \quad (3)$$

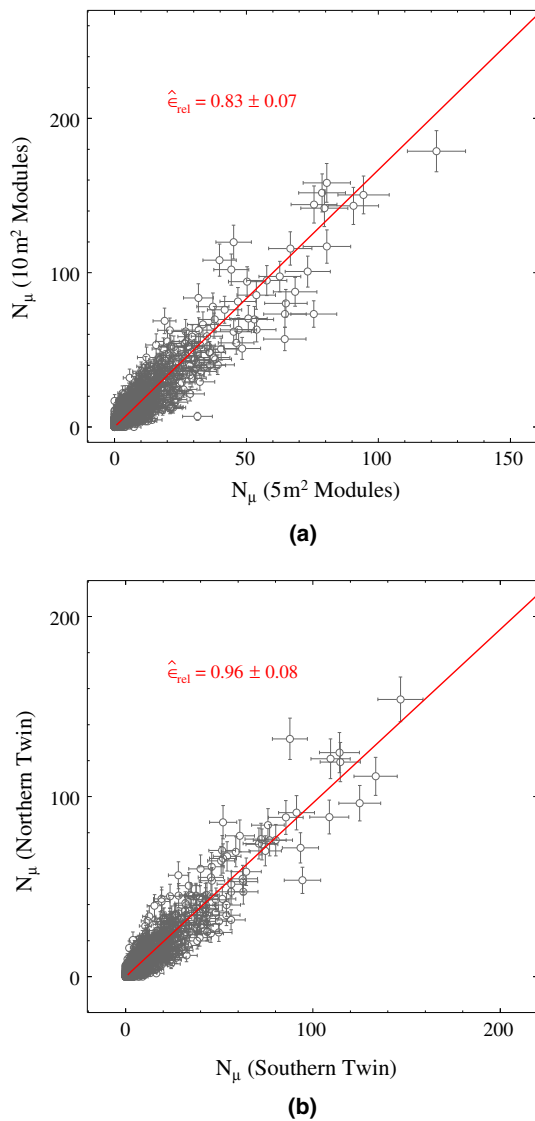


Fig. 6 Relative efficiency from EAS data in twin detectors. **a** Between detectors of different areas (10 m^2 with respect to 5 m^2 modules). **b** Between identical detector areas of 30 m^2 . The estimation of the relative efficiency is obtained from Eq. (5), and its value is used for plotting the red solid line

which leads to

$$\hat{r} = \frac{\sum_{i=1}^N N_{1i}}{\sum_{i=1}^N N_{2i}} = \frac{\bar{N}_1}{\bar{N}_2}, \quad (4)$$

i. e. the ratio of the sample average measured by the detector of area S_1 with respect to the sample average of the detector of area S_2 . Combining Eq. (1) with Eq. (4), the relative efficiency estimator is then

$$\hat{\epsilon}_{\text{rel}} = \frac{S_2}{S_1} \frac{\bar{N}_1}{\bar{N}_2}. \quad (5)$$

In total there are eight modules located at the twin position. Half of them have an area of 10 m^2 and the other half an area of 5 m^2 . The relative efficiency between the detectors can thus be assessed in terms of the measurements over $S_1 = 4 \times 10 \text{ m}^2 = 40 \text{ m}^2$ and $S_2 = 4 \times 5 \text{ m}^2 = 20 \text{ m}^2$. The comparison between muon counts over 10 m^2 modules with respect to 5 m^2 modules is shown in Fig. 6a. The relative efficiency estimation yields $\hat{\epsilon}_{\text{rel}} = 0.83 \pm 0.07$, a value mainly driven by the attenuation of light along the fiber in the modules with larger area. This result is, within uncertainties, compatible with laboratory measurements discussed in Sect. 2.2.

2.4 Resolution

Twin detectors can also be used to determine the resolution of the counting procedure. The muon numbers recorded by the overall 30 m^2 detectors are compared in Fig. 6b. The relative efficiency estimation yields $\hat{\epsilon}_{\text{rel}} = 0.96 \pm 0.08$, a value compatible with 1. Equal-area detectors thus behave as identical ones. This supports the idea that twin detectors can be used to assess the fluctuations of the measured signals in a similar manner to that used in the case of the SD stations [21], as reported with preliminary results in [14, 15]. The underlying principle is that two identical close-by detectors basically measure the same spot of the shower. Therefore, the accuracy of the measurement can be estimated by analyzing the difference of the signals for a given event. Note that to ensure twin detectors sample the same muon density, we consider only signals at least 200 m away from the shower core, so that the change of density due to the $\simeq 20 \text{ m}$ separation of the twins is negligible. Such a cut in distance also limits the fluctuations of the muon density.

To determine the resolution of the UMD detectors for each event, the estimator based on the sample variance σ^2 and mean N_μ is constructed,

$$\Delta^2(N_\mu) = \left(\frac{\sigma}{N_\mu} \right)^2 = 2 \left(\frac{N_1 - N_2}{N_1 + N_2} \right)^2. \quad (6)$$

The variance and mean estimators are calculated from the number of measured muons by each twin detector. The mean value of Δ^2 within bins of average number of muons is shown in Fig. 7a as a function of the muon count. The black line is the result of the fit of a Poisson model to the data. The counting uncertainty results in

$$\Delta^2(N_\mu) = \frac{1.7 \pm 0.9}{N_\mu^{(1.0 \pm 0.2)}}. \quad (7)$$

As an illustration of the behavior of the UMD counters, the bin contents centered on $N_\mu = 5$ in Fig. 7a, are separately displayed in Fig. 7b (northern twin) and in Fig. 7c (southern twin) for a bin width of 1 muon. The results of the Poisson

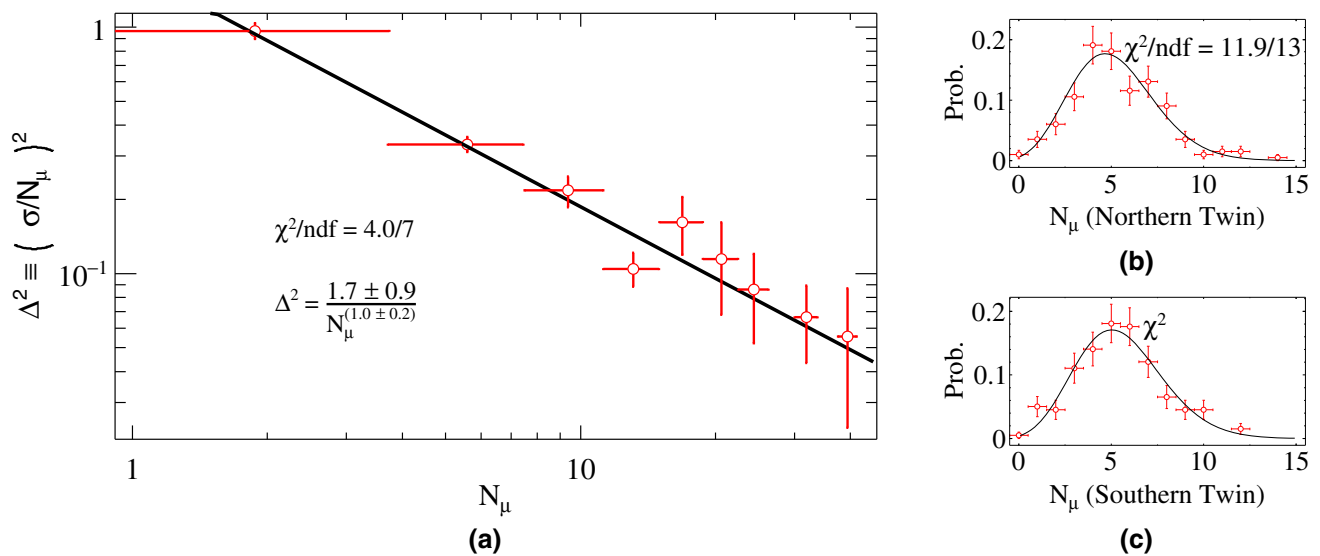


Fig. 7 Resolution of the UMD. **a** The distribution of the mean value of the resolution estimator Δ^2 (see Eq. (6)) within bins of average number of muons. The black line is the fit of a Poisson model to the data. The UMD resembles the ideal behavior of a Poisson detector in this range

fits are shown as the black line. These results support the fact that Δ^2 behaves as N_μ^{-1} , as expected in the case of ideal counters.

3 Measurement of the muon density

3.1 Reconstruction of $\rho(450)$ and ρ_{35}

The first step in the measurement of the muon density with the UMD is the reconstruction of the geometry (arrival direction and position of the impact point) and energy of the EAS with the 750m SD (SD-750) array. The amplitude and the start time of the signals recorded in individual SDs are used to this aim. The arrival direction is determined from the relative arrival times of these signals. The impact point and the energy estimator are then derived by fitting the signal amplitudes to a lateral distribution function (LDF) that decreases monotonically with distance from the shower axis. The energy estimator adopted here is the signal at 450 m from the axis, $S(450)$. For the grid spacing of 750 m, 450 m is the optimal distance to minimize the uncertainties of the signal due to the imperfect knowledge of the functional form of the LDF in individual events. This choice depends essentially on the geometry of the SD array [22,23]. The quantity $S(450)$ is then converted to energy via a calibration against the quasi-calorimetric energy measured by the fluorescence detector. To ensure adequate sampling of the EAS, events with the highest-signal station surrounded by an hexagon of six active stations are used. Then, only those

of signals. From the bin centered around 5 muons, the distribution of counted particles from the northern twin is displayed in **b** and from southern twin in **c**. A Poisson fit to the data is shown in both histograms

with zenith angle $\theta \leq 45^\circ$ and with energies $\geq 2 \times 10^{17}$ eV are selected. The cut in zenith angle allows us to minimize the attenuation effects and the statistical uncertainties due to the reduced scintillation-module detection area, while the cut in energy allows us to work in a regime of the full efficiency of the EAS array. After applying these selection criteria, the data set amounts to 1742 events.

Once the data set is constructed, the measurement of the muon density is based on the signals recorded with the UMD counters. The lateral fall-off of the deposited muon density is modeled with a muon lateral distribution function (MLDF) of perpendicular distance r to the shower axis, $\rho(r)$. This function depends on the primary mass of the cosmic rays. In addition, showers induced by identical primaries at the same energy and at the same incoming angle can be sampled at the ground level at a different age, due to shower-to-shower fluctuations arising from the stochastic variations in the location and character of the leading interactions. This results in natural fluctuations for the MLDF, which is thus a quantity that varies on an event-by-event basis. Unfortunately, the sparse spacing of the array prevents us from measuring the event-by-event LDF so as to use it as the primary input for defining the muon-density estimator. To circumvent this, the strategy to reconstruct the muon density then follows from the same technique as in the case of the estimation of the shower-size parameter $S(450)$ with the SD array. An *average* MLDF is determined from Monte-Carlo simulations of EAS, and the signal deposit of an event is then adjusted to this average MLDF by scaling its normalisation in a fitting procedure.

In this work, to obtain the average MLDF, we have simulated two primaries, protons and iron nuclei, with energies of $10^{17.5}$ eV, $10^{18.0}$ eV, $10^{18.5}$ eV and zenith angles 0° , 12° , 22° , 32° , 38° , 48° , by making use of CORSIKA simulations [24] with two different generators of hadronic interactions, QGSJETII-04 and EPOS-LHC. The secondary particles of the EAS reaching the ground level are subsequently propagated through the soil, and the energy deposited in the underground muon detector is calculated with the GEANT4 [25] package. Finally, the response of the detector is simulated by means of the Pierre Auger Observatory Offline Software Framework [26].

The average MLDF is parameterized as

$$\rho(r, E, \theta) = \rho(450) f(r, \theta), \quad (8)$$

where $\rho(450)$, the signal expected at a radial distance of 450 m, is the muon density estimator that depends on both the energy E and the zenith angle θ . The distance of 450 m has been chosen to minimize the fluctuations of the event-dependent MLDF from the average one. The average structure function, $f(r, \theta)$, is normalized so that $f(r = 450 \text{ m}) \equiv 1$. Its functional shape follows from the KASCADE-Grande experiment [9, 14, 27],

$$f(r, \theta) = \left(\frac{r}{r^*}\right)^{-\alpha} \left(1 + \frac{r}{r^*}\right)^{-\beta} \left[1 + \left(\frac{r}{10r^*}\right)^2\right]^{-\gamma}, \quad (9)$$

where $r^* = 280$ m, $\alpha = 0.3$ and $\gamma = 4.6$. The functional shape adopted for the parameterization of the slope parameter, β , is guided by the application of Linsley's elongation rate theorem [28, 29],

$$\beta(\theta; b_0, b_1) = b_0 + b_1 \sec \theta \quad (10)$$

with $b_0 = 4.4$ and $b_1 = -1.1$. All the values of these fixed parameters, namely, the values of the set $\{r^*, \alpha, \gamma, b_0, b_1\}$, were optimized with the above mentioned simulations.

The expected number of muons, $\mu(r, E, \theta)$, that hit a scintillation module located at a distance r from the impact point of a shower impinging with zenith angle θ is then derived as $\mu(r, E, \theta) = \rho(r, E, \theta) S \cos \theta$, with $S \cos \theta$ the projected aperture of the detectors. The observed number of muons is drawn from a Poisson process with the mean μ . On an event-by-event basis, the value of $\rho(450)$ is therefore estimated by minimizing the likelihood function

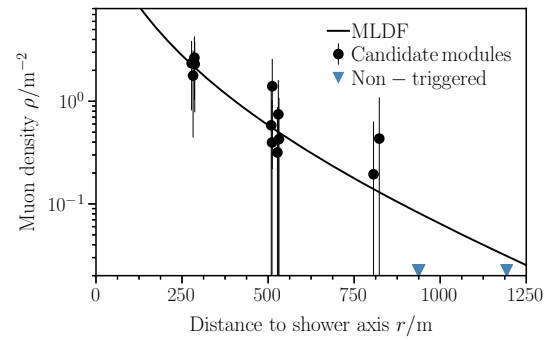


Fig. 8 Example of MLDF fit to a real event

$$\begin{aligned} \mathcal{L} &= \mathcal{L}_{\text{sat}} \times \mathcal{L}_{\text{cand}} \times \mathcal{L}_{\text{non-trg}} \\ &= \prod_{i=1}^{N_{\text{sat}}} \frac{1}{2} \left[1 - \operatorname{erf} \left(\frac{N_i - \mu(r_i)}{\sqrt{2\mu(r_i)}} \right) \right] \\ &\quad \times \prod_{i=1}^{N_{\text{cand}}} e^{-\mu(r_i)} \frac{\mu(r_i)^{N_i}}{N_i!} \\ &\quad \times \prod_{i=1}^{N_{\text{non-trg}}} e^{-\mu(r_i)} \left(1 + \mu(r_i) + \frac{1}{2} \mu(r_i)^2 \right), \end{aligned} \quad (11)$$

consisting of the product of the likelihoods for saturated, non-saturated (or *candidate*) and non-triggered UMD stations [30]. The likelihood for the non-triggered stations is built from the probability not to trigger when there are less than three muons hitting the UMD. This upper limit comes from the water-Cherenkov detector condition which requires at least a signal of 3 Vertical Equivalent Muons (VEMs) to trigger. The value N_i is the effective number of muons reconstructed by each scintillation module, namely

$$N_i = \sum_{j=1, k_j \neq 64}^m -64 \ln \left(1 - \frac{k_j}{64} \right), \quad (12)$$

where k_j is the number of scintillator bars, in a module of 64 strips, for which at least one muon in the j -th time window was reconstructed. The time width of the window is ~ 22 ns and the index j runs over all m windows in an event of 6.4 μ s. As soon as any of the k_j equals 64, the module is considered as saturated and the corresponding N_i value is used as a lower limit for the observed number. This reconstruction procedure is illustrated in Fig. 8, where the MLDF is fitted to the observed muon numbers. The density for non-triggered modules is set, arbitrarily, to 10^{-2} m^{-2} .

As a result of the longer path in the atmosphere and of the increased amount of soil covering the detectors, the muonic component of inclined EAS gets attenuated. Consequently, the last step consists in correcting the muon density estimator for the attenuation. Given the highly isotropic flux,

Table 1 Systematic uncertainties associated with the measurement of the muon density

Source of uncertainty	Systematic uncertainty %
Calibration	3.9
Soil density	2.8
MLDF	8.8
Efficiency correction	9.9
CIC correction	2.3
Total	14.3

the intensity of primary cosmic rays is expected to be θ -independent. Deviations from an isotropic intensity can thus be interpreted as being due to attenuation alone. Based on this principle, an empirical procedure, known as the constant intensity cut (CIC) method [31], is used to determine the attenuation curve f_{att} as a function of θ and therefore an attenuation-free muon density, $\rho_{35} = \rho(450)/f_{\text{att}}(\theta)$, arbitrarily defined at 35° as in the case of the SD array. The attenuation function f_{att} is parameterized as $f_{\text{att}}(\theta) = 1 + ax + bx^2$, with $x = \cos^2 \theta - \cos^2 35^\circ$. The obtained parameters are $a = 0.54 \pm 0.10$ and $b = -1.02 \pm 0.69$.

3.2 Systematic uncertainties

The following systematic uncertainties have been studied in detail: (i) the calibration procedure, (ii) the density variations of the soil covering the area of the detector array, (iii) the unknown shape of the MLDF, (iv) the module area-dependent efficiency correction, and (v) the CIC correction of the muon density $\rho(450)$. The impact of each source of uncertainty is summarized in Tab. 1.

Calibration procedure. As described in Sect. 2.2, the purpose of the calibration of the array equipped with photomultiplier tubes is to set the threshold of discrimination (V_{Thr}) of each PMT channel at the level of 30% of the mean single photo-electron amplitude (V_{SPE}). In the engineering UMD array there are in total 2240 channels. The spread of thresholds after calibration is 21 mV, which corresponds to about 10% of the discriminator threshold. The detector response has been simulated with proton and iron showers of 10^{18} eV generated with QGSJETII-04 at two zenith angles for different values of V_{Thr} , ranging from 20% to 40% of V_{SPE} , to estimate the effect of a 3σ variation. The relative difference in the reconstruction of $\rho(450)$ for different thresholds is shown in Fig. 9a. A systematic uncertainty of 3.9% is obtained from the linear fit.

Soil density. Variations in the soil density over the 23.5 km^2 of the SD-750 array add further systematic uncertainties. The shielding of the electromagnetic component of EAS as well as the energy of the muons that can reach the underground detectors depend on the density of the soil. In-situ

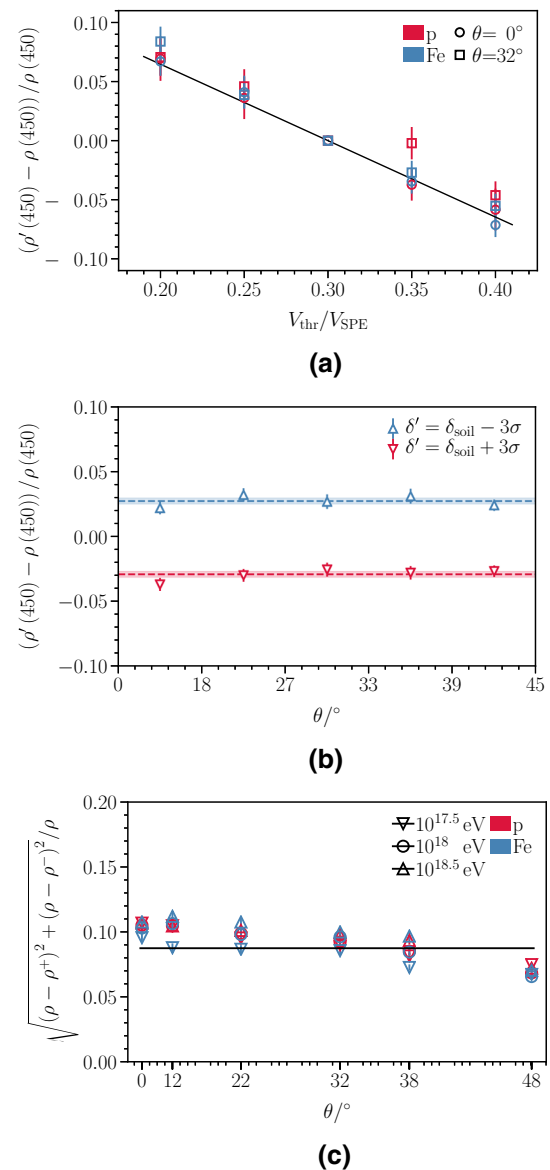


Fig. 9 Relative difference of the reconstructed $\Delta\rho(450)$ obtained with QGSJETII-04, for proton and iron: **a** for different thresholds of discrimination, up to $\pm 10\%$ of the appointed value of $0.3 \times V_{\text{SPE}}$, at an energy of 10^{18} eV, and for two zenith angles; **b** for soil density variations of 3σ around the measured mean value of $\delta_{\text{soil}} = 2.380 \text{ g/cm}^3$ in bins of shower zenith angle θ ; and **c** for variations of $\pm 15\%$ of the slope parameter β as function of θ at different energies

measurements of the density in three positions (two in the periphery and one in the center) of the SD-750 array were performed at depths of 1 m, 2 m, and 3 m. The mean measured soil density was $\delta_{\text{soil}} = 2.380 \text{ g/cm}^3$ with a dispersion of $\sigma_\delta = 0.051 \text{ g/cm}^3$ between surveyed sites. The relative differences in the reconstructed muon densities at 450 m for $3\sigma_\delta$ variations are shown in Fig. 9b as a function of the shower zenith angle θ . The dashed lines are the difference averaged over all angles, and shaded bands represent the standard error

of the mean. Averaged over all considered angles, a systematic uncertainty of 2.8% is found.

Lateral distribution function. The event-by-event fluctuations in the actual shape of the MLDF adds additional systematic uncertainties. From Monte-Carlo simulations, a conservative estimation can be made by varying the slope parameter β within a determined dispersion. The value for the dispersion, $\sigma_\beta = 0.15 \beta$, was selected by using a small set of simulated events with sufficient detector information to leave β as a free fit parameter during the reconstruction procedure. For this set, we compared the value of β obtained from the fit and the one obtained by using formula 10. The estimated result was a 15% difference. As an illustration, the mean relative uncertainty obtained with QGSJETII-04 is shown as a function of θ in Fig. 9c. Mean values are shown as the markers, while error bars stand for their dispersion. Averaging over all angles, a relative systematic uncertainty of 8.8% is obtained.

Module efficiency correction. During the reconstruction procedure, the estimated muon densities were corrected, by area-dependent efficiencies ϵ , according to $\rho^{\text{corr}} = \rho / \epsilon$. The values for ϵ used were selected accordingly to the optimized time window of seven bins. As was shown in Sect. 2.2, $\epsilon_5(7) = 1.04$ and $\epsilon_{10}(7) = 0.95$ for modules of 5 m^2 and 10 m^2 , respectively. We evaluate the resulting systematic uncertainty by reconstructing $\rho(450)$ for each event in data, both for the efficiencies derived for a window size of seven bins and for the case in which no inhibition window is set ($\epsilon_5(\infty) = 0.94$ and $\epsilon_{10}(\infty) = 0.87$ according to laboratory measurements). Averaged over the considered energy range from $2 \times 10^{17} \text{ eV}$ to $2 \times 10^{18} \text{ eV}$, we find a conservative systematic uncertainty of 9.9%.

CIC correction. We consider as systematic uncertainty associated to the CIC correction the uncertainties on the parameters of the fit. Averaged over the zenith angle range $0^\circ \leq \theta \leq 45^\circ$, the mean systematic uncertainty is 2.3%.

4 Evolution of the muon content as a function of energy

4.1 Results

The reconstructed muon densities ρ_{35} are shown in Fig. 10 as a function of the energy estimated by using the SD data alone. Due to the steep energy spectrum, the number of events runs out of statistics above $\approx 2 \times 10^{18} \text{ eV}$. With the current sensitivity of the Auger X_{max} measurements in the energy range of interest here, namely between $\approx 2 \times 10^{17} \text{ eV}$ and $\approx 2 \times 10^{18} \text{ eV}$, a constant elongation rate (that is, a single logarithmic dependence of X_{max} with energy) is observed [32]. In this case, a single power law dependence of ρ_{35} with energy is expected from Monte-Carlo simulations. We thus

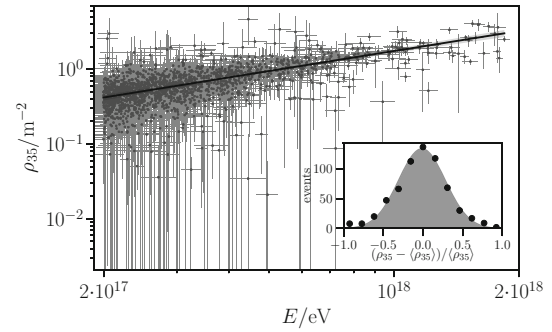


Fig. 10 Muon densities ρ_{35} as a function of the energy. The distribution of the normalized residuals $(\rho_{35} - \langle \rho_{35} \rangle) / \langle \rho_{35} \rangle$ is shown in the inset

describe the correlation between ρ_{35} and E by a power-law function,

$$\rho_{35}(E; A, B) = A \times (E/10^{18} \text{ eV})^B, \quad (13)$$

where the average muon density at 10^{18} eV , A , and the logarithmic gain, B , are fitted to data. In this manner, the correlation expressed through this power-law relationship provides an unbiased estimate of the mean evolution of ρ_{35} with energy, averaged over the underlying mass distribution.

The correlation fit is carried out using a tailored maximum likelihood method allowing various effects of experimental origin to be taken into account, in a manner similar to that described in [33]. The probability density function, $p(\rho_{35}, E_{\text{SD}})$, entering the likelihood procedure, is built by folding the cosmic-ray spectrum $J(E)$, observed with the effective exposure of the SD proportional to its detection efficiency $\epsilon_{\text{SD}}(E)$, with the resolution functions of the SD, $R_{\text{SD}}(E_{\text{SD}}|E, \sigma_{\text{SD}})$, and of the UMD, $R_{\text{UMD}}(\rho_{35}|\rho, \sigma_{\text{UMD}})$:

$$p(\rho_{35}, E_{\text{SD}}) \propto \int dE \int d\rho R_{\text{SD}}(E_{\text{SD}}|E) R_{\text{UMD}}(\rho_{35}|\rho) \times \epsilon_{\text{SD}}(E) \epsilon_{\text{UMD}}(\rho) J(E) \delta(\rho, \rho(E)). \quad (14)$$

Here, the Dirac function guarantees that the power-law relationship between the underlying muon density ρ and energy E values holds, the parameters of which are estimated through equation (13). The parameters σ_{SD} and σ_{UMD} model the resolutions in E_{SD} and ρ_{35} , respectively. Shower to shower fluctuations are accounted for in σ_{SD} . The statistical uncertainty for σ_{UMD} of a single event is calculated by bootstrapping 50 times the measured scintillation module data pairs $(r_i, \rho(r_i))$. Repeating the MLDF fitting procedure for the bootstrapped sample of the same event, we estimate σ_{UMD} as the standard deviation of the obtained distribution of ρ_{35} . For underlying muon-density values, ρ_{35} , high enough so that the detection efficiency of the UMD is close to 1, and by making use of a bootstrap estimate of the underlying spectrum observed through the SD, $\epsilon_{\text{SD}}(E) J(E) \propto \sum_i \delta(E, E_{\text{SD}i})$,

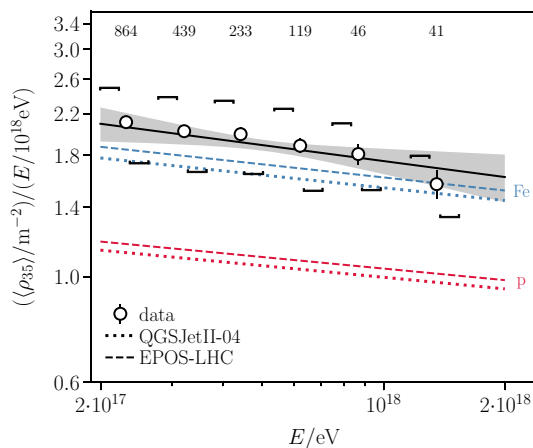


Fig. 11 Energy-normalized muon densities $\langle \rho_{35} \rangle / (E/10^{18} \text{ eV})$ as a function of E compared to expectations from simulations using EPOS-LHC (dashed) and QGSJETII-04 (dotted). Error bars denote the statistical uncertainties, while systematic uncertainties are indicated by square brackets

the p.d.f. reduces to a discrete sum over the events:

$$p \simeq \frac{1}{N_{\text{tot}}} \sum_{i=1}^{N_{\text{tot}}} R_{\text{SD}}(E_{\text{SD}} | E_{\text{SD}i}, \sigma_{\text{SD}i}) \times R_{\text{UMD}}(\rho_{35} | \rho_{35}(E_{\text{SD}i}), \sigma_{\text{UMD}i}). \quad (15)$$

Using the relationship of equation (13), the coefficients A and B are then determined maximizing the log-likelihood function $\ln \mathcal{L}(A, B) = \sum_{k=1}^N p(\rho_{35k}, E_{\text{SD}k})$ where N is the number of events above $10^{17.3} \text{ eV}$. Note that, as a remnant of the integration over energy between 0 and infinity in equation (14), the sum over the N_{tot} events entering into equation (15) extends to lower energies to capture the fluctuations of the energy estimator. The best fit solution is shown as the solid line in Fig. 10, obtained for the best-fit parameters

$$A = (1.75 \pm 0.05(\text{stat.}) \pm 0.05(\text{sys.})) \text{ m}^{-2}, \quad (16)$$

$$B = 0.89 \pm 0.04(\text{stat.}) \pm 0.04(\text{sys.}). \quad (17)$$

The statistical parameter uncertainties have been calculated by generating 1000 balanced bootstraps from the data set, repeating the fit for every bootstrap sample, and calculating the standard deviations from fit results. The distribution of the normalized residuals $(\rho_{35} - \langle \rho_{35} \rangle) / \langle \rho_{35} \rangle$ is shown in the inset of Fig. 10.

The evolution of the muon content in data is compared to that in simulations of proton (in red) and iron (in blue) primaries in Fig. 11, bracketing the lightest and heaviest cosmic-ray primaries. The muon densities are normalized by the energy to soften most of the energy scaling and thus emphasize the effect of the primary mass on the muon number. The number of events in each energy bin is stated at the top of the figure. The statistical uncertainties are shown

as the error bars, propagating the correlation between ρ_{35} and E , while the square brackets stand for the systematic uncertainties. The impact of the systematic uncertainty in the SD energy estimate, amounting to 14%, is shown by the diagonal shift of the square brackets. The obtained fit curve is shown as the black solid line with a shaded band corresponding to the statistical uncertainties. Simulation results have been obtained by making use of two leading LHC-tuned high-energy hadronic interaction models, namely EPOS-LHC (dashed) and QGSJETII-04 (dotted). The gain parameters, B , obtained from both hadronic interaction models are $B = 0.91$ for iron and $B = 0.92$ for proton primaries, consistent within uncertainties to those obtained from data.

However, the observed muon densities are larger in data than those predicted by the models. For instance, in the extreme case of a pure iron composition, the observed values are between 8% (EPOS-LHC) and 14% (QGSJETII-04) larger than those predicted at 10^{18} eV . We note however that a shift of the data points within the systematic uncertainties is enough to bring them in the region of the iron primaries. These systematic uncertainties are mainly inherited from the energy scale uncertainty [34]. They appear to be the limiting factor to use ρ_{35} as a mass-composition estimator, but we show next the power of the ρ_{35} measurements to probe the consistency of hadronic interaction generators to model the development of EASs.

4.2 Combination with other measurements

The muon density is sensitive to the primary mass composition. The above result can thus be used to test the ability of the hadronic interaction models to describe air showers by comparing it with that expected from the primary composition extracted in an independent way. Thanks to the hybrid nature of the Pierre Auger Observatory, such an independent mass-composition estimate is inferred from measurements of the mean depth of shower maximum $\langle X_{\text{max}} \rangle$ [32].

The most prominent mass-sensitive tracer is X_{max} , a quantity directly observed with fluorescence detectors. It strongly depends on the primary particle interaction with air nuclei through the inelastic cross section and the multi-particle production, in particular through high-energy neutral pions which decay into photons at high energies. In this regard, models maximally benefit from the studies of proton-proton and proton-nucleus collisions at the LHC. By contrast, the muon content of EASs stems from a multi-step cascade process, mostly driven by interactions of secondary charged pions and kaons with air. ρ_{35} thus depends on properties of pion-air collisions over a wide range of energies, for which a detailed knowledge is lacking.

Furthermore, in the framework of the generalised Heitler model, both quantities can be related to the mean logarithmic mass ($\ln A$) through a linear dependence. Consequently,

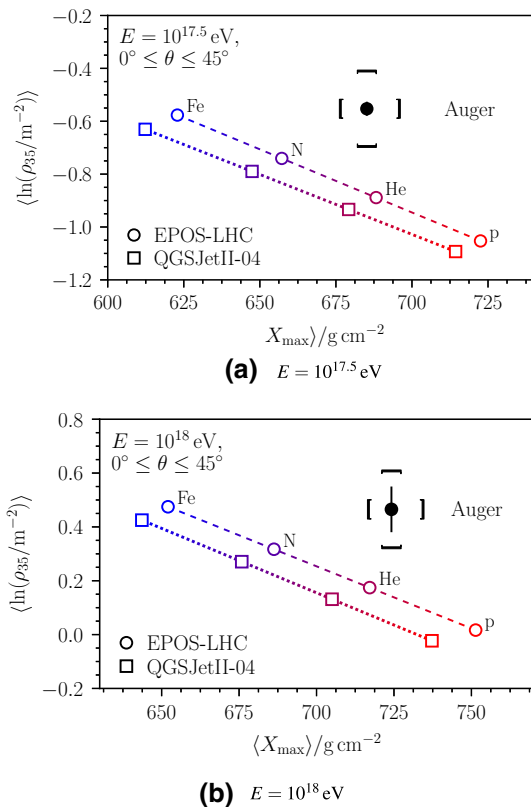


Fig. 12 Mean logarithmic muon density $\langle \ln \rho_{35} \rangle$ as a function of the mean depth of shower maximum $\langle X_{\max} \rangle$ for simulations with primary energies of $10^{17.5}$ eV (a) and 10^{18} eV (b) compared to Auger Observatory measurements with the FD

the relationship between $\langle X_{\max} \rangle$ and $\langle \ln \rho_{35} \rangle$ can be represented by a line for each hadronic interaction model, as shown in Fig. 12 at two different energies, $10^{17.5}$ eV and 10^{18} eV. The $\langle X_{\max} \rangle$ data are extracted from [32]. It is apparent that both models fail to reproduce the data. A difference of 38% in the muon number is observed at $10^{17.5}$ eV and 10^{18} eV compared to EPOS- LHC predictions, while the difference is larger compared to the QGSJETII- 04 predictions. In both cases, data show that the analyzed hadronic interaction models produce fewer muons than those observed in EAS. All these results are collected in Tab. 2 together with the corresponding statistical and systematic uncertainties. It should be stressed, nevertheless, that in the above comparison the true Monte-Carlo energy was used for the simulated data because the hybrid reconstruction of the energy (as done for real data) is hampered by the failure in reproducing the number of muons impinging the SD stations [35].

The results presented in Figs. 10 and 11 are the first ones for the Pierre Auger Observatory on the muon content of the air showers obtained in this energy range. They allow us to extend to lower energies results previously reported at higher energies, based on the muon number estimation in inclined air showers [36,37]. This is because at zenith angles exceed-

Table 2 Ratio $f_{\mu} = \exp(\langle \ln \rho_{35} \rangle_{\text{UMD}} - \langle \ln \rho_{35} \rangle_{\text{sim}})$ of the muon content in data and simulations with statistical and systematic uncertainties at primary energies of $10^{17.5}$ eV and 10^{18} eV for the EPOS- LHC and QGSJETII- 04 hadronic interaction models

Energy	Model	f_{μ}
$10^{17.5}$ eV	EPOS- LHC	$1.38 \pm 0.04(\text{stat}) \pm {}^{0.21}_{0.18}(\text{sys})$
	QGSJETII- 04	$1.50 \pm 0.04(\text{stat}) \pm {}^{0.23}_{0.20}(\text{sys})$
$10^{18.0}$ eV	EPOS- LHC	$1.38 \pm 0.12(\text{stat}) \pm {}^{0.21}_{0.18}(\text{sys})$
	QGSJETII- 04	$1.53 \pm 0.13(\text{stat}) \pm {}^{0.23}_{0.20}(\text{sys})$

ing $\approx 60^\circ$, EASs provide a direct measurement of the muon number at the ground due to the absorption of the electromagnetic component in the large atmospheric depth traversed. The muon number for each shower can then be derived by scaling a simulated reference profile of the muon density distribution at the ground to the data. It is worth noting that the measurements obtained pertain to muons with energies above 0.16 GeV (Cherenkov threshold in water) that reach the Observatory site located at an altitude of 1425 m, while the measurements obtained in this work pertain to muons with energies ~ 1 GeV for vertical incidence.

Given the different conditions of measurements that select muons with different energy distributions, it proves difficult to compare directly the results presented here and the ones reported in [36,37]. An indirect manner is required. Following [38], we make use of the z -scale factor to perform the comparisons,

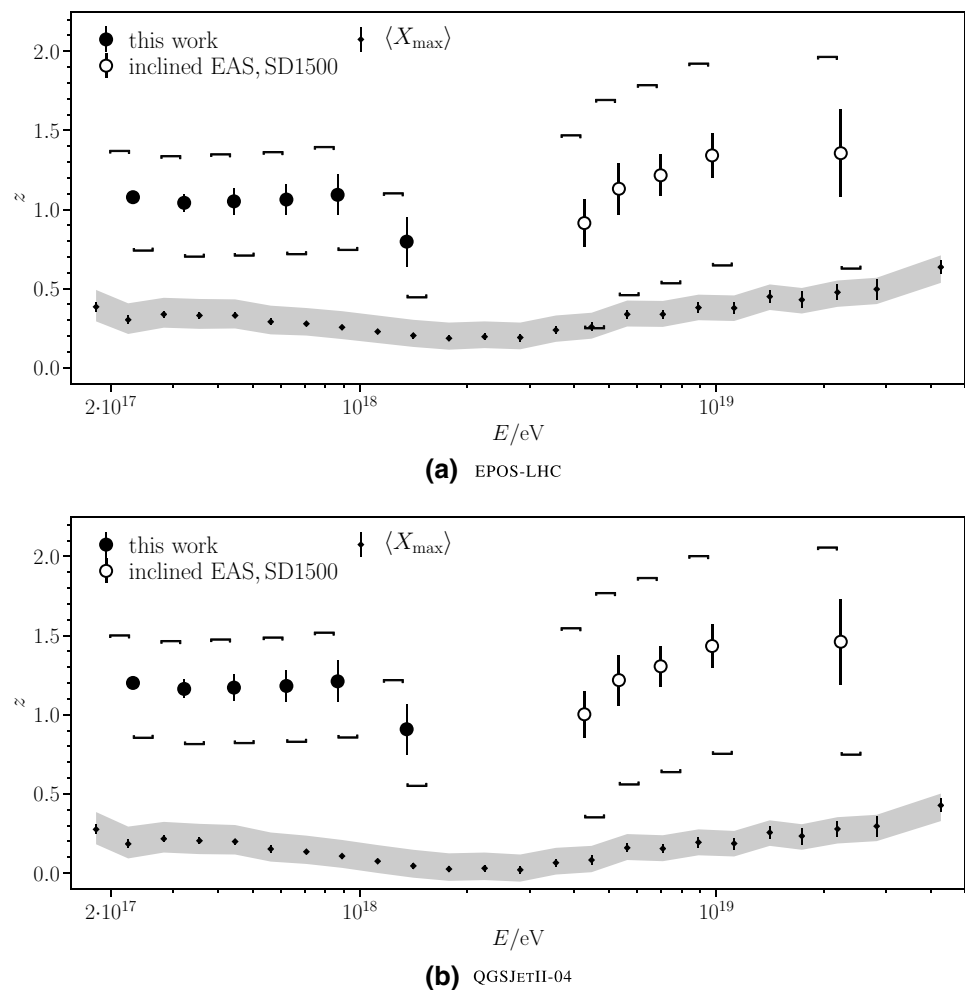
$$z = \frac{\langle \ln x \rangle - \langle \ln x \rangle_{\text{p}}}{\langle \ln x \rangle_{\text{Fe}} - \langle \ln x \rangle_{\text{p}}} \quad (18)$$

where x is the muon-density estimator (that is, ρ_{35} in this work and R_{μ} in [37]). Here, the symbols $\langle \cdot \rangle_{\text{p}}$ and $\langle \cdot \rangle_{\text{Fe}}$ stand for the expected muon densities for proton and iron showers, simulated with a given model and accounting for detector effects. The normalization by the difference between iron and proton simulations allows the comparison between different types of quantities by reducing the possible systematic differences.

The results of both analyses are shown in Fig. 13, using two distinct generator models of hadronic interactions to predict $\langle \ln \rho_{35} \rangle$ for proton and iron: EPOS- LHC (a) and QGSJETII- 04 (b). There is a gap between $\approx 2 \times 10^{18}$ eV (UMD-based analysis running out of statistics) and $\approx 4 \times 10^{18}$ eV (threshold of the inclined EAS-based analysis), but overall, both analyses give similar results in terms of z -factor.

Assuming the validity of the superposition model, the measurement of $\langle X_{\max} \rangle$ by the FD converted into an average logarithmic mass $\langle \ln A \rangle$ and finally into $z = \langle \ln A \rangle / \ln 56$ can be used to establish the reference values of the z -factor. These are shown as the diamond markers in Fig. 13. For

Fig. 13 z -factor obtained from this work (filled circles) and from measurements of inclined EASs higher in energy by a decade and a half (open circles) for the EPOS-LHC (a) and the QGSJETII-04 (b) hadronic interaction models. Also shown in both cases are the results obtained from measurements of the mean depth of shower maximum (X_{\max}) by the FD



an ideal hadronic interaction model, the z -factor measured from muon densities should be consistent with that inferred from composition data. However, a clear tension is observed between the two types of measurement. This tension is higher in the lower energy range explored here than in that studied with inclined EASs, due to the smaller uncertainties, being at the level of 2.0σ and 2.5σ confidence for the EPOS-LHC and QGSJETII-04 models, respectively, at 2×10^{17} eV. The hadronic interaction models thus fail to reproduce consistently the z -scale factor inferred from muon-based and $\langle X_{\max} \rangle$ -based measurements. On the other hand, the logarithmic gains of muon-based and $\langle X_{\max} \rangle$ -based measurements show comparable trends with energy although the large uncertainties of the muon-based data points prevent us from drawing any firm statement.

Overall, the discrepancy in muon number captured in this work, down to 2×10^{17} eV, extends the previously reported one at higher energies. It is worth keeping in mind, however, that these results are sensitive to a change of energies. A positive shift of our energy scale within its systematic uncer-

tainties would reduce the tensions on the muon numbers. In another study, we reported on a simultaneous fit of the longitudinal development and of the LDF for events with energy between 6×10^{18} and 1.6×10^{19} eV detected by the SD and the FD [35]. Agreement of models with data is obtained on the condition to increase the hadronic contribution to the signals by an amount consistent with that reported in [35] on the one hand, and to leave the energy scale unchanged on the other hand. The uncertainty on the energy rescaling factor is of the same order of magnitude as the 14% systematic uncertainty of the energy calibration, though.

Similar results were previously obtained by other experiments such as Yakutsk [39] and HiRes/MIA [40]. More recently, a joint study with data from SUGAR and Auger also confirmed qualitatively these findings [41], as well as a study at the Telescope Array [42]. A meta-analysis combining all these results was done [10], confirming the trend that the muon deficit in the simulation is probably increasing with energy.

5 Summary and conclusions

The studies presented in this work are the final results of the engineering array phase of the UMD. This prototype array was composed of seven stations organized in a hexagon. After a period for the development of calibration routines, data acquisition for performance and physics started by the end of 2015. The engineering array phase concluded in November 2017 when several hardware improvements were implemented according to the final production design of the UMD. The most notable upgrade is the selection of silicon photo-multipliers rather than photo-multiplier tubes as optical devices.

Using data from a period of stable operation of one year, it has been demonstrated that the detectors resemble the behavior of ideal Poisson counters. The assessed resolution was $\propto 1/N_\mu^{(1.0 \pm 0.2)}$.

Systematic uncertainties have been studied in detail. The largest contribution (9.9%) arises from the area-dependent efficiency correction of the muon densities recorded by individual detector modules. The uncertainties due to the calibration procedure (3.9%), variations in the soil density (2.8%), the lack of knowledge of the shape of the muon lateral distribution function for single events (8.8%), and the CIC correction (2.3%) were also considered, yielding an overall systematic uncertainty of 14.3%.

In the covered energy range, namely between 2×10^{17} eV and 2×10^{18} eV, the observed muon densities are larger than those expected from Monte-Carlo simulations of EAS when considering the mass composition inferred from $\langle X_{\max} \rangle$ measurements. The disagreement between the muon content reported in this study and that expected from simulations can be summarized in the following way: we find that for the EPOS-LHC model to explain the data an increase of 38% is required at $10^{17.5}$ eV and 10^{18} eV, while for QGSJETII-04 an increment of 50% and 53% is needed at the two energies, respectively. Converting the measured muon densities into the z -factor described in Section 4, the results obtained here allow us to extend to lower energies muon-number measurements conducted at the Observatory, based on the detection of horizontal air showers at higher energies. The energy evolution (logarithmic gain) of the different muon measurements is consistent, within uncertainties, with that expected from $\langle X_{\max} \rangle$ measurements. Overall, these results provide important constraints for hadronic interaction models to describe the EAS development.

The full-sized UMD array with 61 stations is foreseen to be completed in 2022. It will provide direct measurements of the muon component of EAS in the energy range above 10^{17} eV. Therefore, it will overlap around $10^{18.5}$ eV with observations from the 1500m array. The UMD detector will enable the validation and fine-tuning of the methods that will allow for disentangling the electromagnetic and muonic compo-

nents on an event-by-event basis with the upgraded version of the Auger Observatory [43]. Ultimately, these measurements will allow an accurate analysis of mass-sensitive parameters on an event-by-event basis, to help elucidate the origin of cosmic rays at the highest energies.

Acknowledgements The successful installation, commissioning, and operation of the Pierre Auger Observatory would not have been possible without the strong commitment and effort from the technical and administrative staff in Malargüe. We are very grateful to the following agencies and organizations for financial support: Argentina – Comisión Nacional de Energía Atómica; Agencia Nacional de Promoción Científica y Tecnológica (ANPCyT); Consejo Nacional de Investigaciones Científicas y Técnicas (CONICET); Gobierno de la Provincia de Mendoza; Municipalidad de Malargüe; NDM Holdings and Valle Las Leñas; in gratitude for their continuing cooperation over land access; Australia – the Australian Research Council; Brazil – Conselho Nacional de Desenvolvimento Científico e Tecnológico (CNPq); Financiadora de Estudos e Projetos (FINEP); Fundação de Amparo à Pesquisa do Estado de Rio de Janeiro (FAPERJ); São Paulo Research Foundation (FAPESP) Grants No. 2019/10151-2, No. 2010/07359-6 and No. 1999/05404-3; Ministério da Ciência, Tecnologia, Inovações e Comunicações (MCTIC); Czech Republic – Grant No. MSM CR LTT18004, LO1305, LM2015038 and CZ.02.1.01/0.0/0.0/16_013/0001402; France – Centre de Calcul IN2P3/CNRS; Centre National de la Recherche Scientifique (CNRS); Conseil Régional Ile-de-France; Département Physique Nucléaire et Corpusculaire (PNC-IN2P3/CNRS); Département Sciences de l'Univers (SDU-INSU/CNRS); Institut Lagrange de Paris (ILP) Grant No. LABEX ANR-10-LABX-63 within the Investissements d'Avenir Programme Grant No. ANR-11-IDEX-0004-02; Germany – Bundesministerium für Bildung und Forschung (BMBF); Deutsche Forschungsgemeinschaft (DFG); Finanzministerium Baden-Württemberg; Helmholtz Alliance for Astroparticle Physics (HAP); Helmholtz-Gemeinschaft Deutscher Forschungszentren (HGF); Ministerium für Innovation, Wissenschaft und Forschung des Landes Nordrhein-Westfalen; Ministerium für Wissenschaft, Forschung und Kunst des Landes Baden-Württemberg; Italy – Istituto Nazionale di Fisica Nucleare (INFN); Istituto Nazionale di Astrofisica (INAF); Ministero dell'Istruzione, dell'Università e della Ricerca (MIUR); CETEMPS Center of Excellence; Ministero degli Affari Esteri (MAE); México – Consejo Nacional de Ciencia y Tecnología (CONACYT) No. 167733; Universidad Nacional Autónoma de México (UNAM); PAPIIT DGAPA-UNAM; The Netherlands – Ministry of Education, Culture and Science; Netherlands Organisation for Scientific Research (NWO); Dutch national e-infrastructure with the support of SURF Cooperative; Poland -Ministry of Science and Higher Education, grant No. DIR/WK/2018/11; National Science Centre, Grants No. 2013/08/M/ST9/00322, No. 2016/23/B/ST9/01635 and No. HARMONIA 5–2013/10/M/ST9/00062, UMO-2016/22/M/ST9/00198; Portugal – Portuguese national funds and FEDER funds within Programa Operacional Factores de Competitividade through Fundação para a Ciência e a Tecnologia (COMPETE); Romania – Romanian Ministry of Research and Innovation CNCS/CCCDI-UESFISCDI, projects PN-III-P1-1.2-PCCDI-2017-0839/19PCCDI/2018 and PN18090102 within PNCDI III; Slovenia – Slovenian Research Agency, grants P1-0031, P1-0385, I0-0033, N1-0111; Spain – Ministerio de Economía, Industria y Competitividad (FPA2017-85114-P and FPA2017-85197-P), Xunta de Galicia (ED431C 2017/07), Junta de Andalucía (SOMM17/6104/UGR), Feder Funds, RENATA Red Nacional Temática de Astropartículas (FPA2015-68783-REDT) and María de Maeztu Unit of Excellence (MDM-2016-0692); USA – Department of Energy, Contracts No. DE-AC02-07CH11359, No. DE-FR02-04ER41300, No. DE-FG02-99ER-41107 and No. DE-SC0011689; National Science Foundation, Grant

No. 0450696; The Grainger Foundation; Marie Curie-IRSES/EPLAN-ET; European Particle Physics Latin American Network; and UNESCO.

Data Availability Statement This manuscript has no associated data or the data will not be deposited. [Authors' comment: All datasets on which the conclusions of the paper rely, are available to readers in the Pierre Auger Observatory web: <https://www.auger.org/index.php/science/data>.]

Open Access This article is licensed under a Creative Commons Attribution 4.0 International License, which permits use, sharing, adaptation, distribution and reproduction in any medium or format, as long as you give appropriate credit to the original author(s) and the source, provide a link to the Creative Commons licence, and indicate if changes were made. The images or other third party material in this article are included in the article's Creative Commons licence, unless indicated otherwise in a credit line to the material. If material is not included in the article's Creative Commons licence and your intended use is not permitted by statutory regulation or exceeds the permitted use, you will need to obtain permission directly from the copyright holder. To view a copy of this licence, visit <http://creativecommons.org/licenses/by/4.0/>. Funded by SCOAP³.

References

1. J. Matthews, *Astrop. Phys.* **22**, 387 (2005)
2. T. Pierog, in *35th ICRC* (Bexco, Korea), PoS(ICRC2017) **1100**
3. P.R. Blake et al., *J. Phys. G: Nucl. Part. Phys.* **21**, 129 (1995)
4. S.P. Knurenko et al., *Int. J. Mod. Phys. A* **20**, 6900 (2005)
5. N. Hayashida et al., *J. Phys. G Nucl. Part. Phys.* **21**, 1101 (1995)
6. M. Aglietta et al., *Astropart. Phys.* **21**, 583 (2004)
7. G. Khristiansen et al., *Astropart. Phys.* **2**, 127 (1994)
8. T. Antoni et al., *Astropart. Phys.* **16**, 373 (2002)
9. W.D. Apel et al., *Nucl. Instrum. Methods A* **620**, 202 (2010)
10. L. Cazon for the for the EAS-MSU, IceCube, KASCADE-Grande, NEVOD-DECOR, Pierre Auger, SUGAR, Telescope Array, and Yakutsk EAS Array collaborations, in *36th ICRC* (Madison, USA), PoS(ICRC2019) **214**
11. The Pierre Auger Collaboration, *Nucl. Instrum. Methods A* **523**, 50 (2004)
12. The Pierre Auger Collaboration, *Nucl. Instrum. Methods A* **798**, 172 (2015)
13. J. M. Figueira for the Pierre Auger Collaboration, in *35th ICRC* (Bexco, Korea), PoS(ICRC2017) **396**
14. B. Wundheiler for the Pierre Auger Collaboration, in *34th ICRC* (The Hague, The Netherlands), PoS(ICRC2015) **324**
15. S. Maldera for the Pierre Auger Collaboration, in *33th ICRC* (Rio de Janeiro, Brazil), **748**
16. F. Suarez for the Pierre Auger Collaboration, in *33th ICRC* (Rio de Janeiro, Brazil), **396**
17. The Pierre Auger Collaboration, *JINST* **11**, P02012 (2016)
18. The Pierre Auger Collaboration, *JINST* **12**, P03002 (2014)
19. B. Wundheiler, for the Pierre Auger Collaboration, in *32th ICRC* (Beijing, China, 2011), **341**
20. S. Müller for the Pierre Auger Collaboration, in *UHECR Conf.* (Paris, France, 2018), EPJ Web Conf. **210**, 02013
21. M. Ave et al., *Nucl. Instrum. Meth. A* **578**, 180 (2007)
22. A.M. Hillas, in *Acta Phys. Acad. Sci. Hung. 29 (Suppl. 3)* (1970)
23. D.W. Newton, et al., *Astropart. Phys.* **26**, 414 (2007)
24. D. Heck, et al., *FZKA-6019* (1998)
25. S. Agostinelli et al., *Nucl. Instrum. Methods A* **506**, 250 (2003)
26. S. Argiro et al., *Nucl. Instrum. Meth. A* **580**, 1485 (2007)
27. F. A. Sánchez for the Pierre Auger Collaboration, in *36th ICRC* (Madison, USA), PoS(ICRC2019) **411**
28. J. Linsley, in *ICRC* (Plovdiv, Bulgaria, 1977)
29. T.K. Gaisser et al., in *ICRC, Kyoto, Japan* (1979)
30. D. Ravnani, A.D. Supanitsky, *Astrop. Phys.* **65**, 1 (2015)
31. J. Hersil et al., *Phys. Rev. Lett.* **6**, 22 (1961)
32. J. Bellido for the Pierre Auger Collaboration, in *35th ICRC* (Bexco, Korea), PoS(ICRC2017) **506**
33. H. Dembinski et al., *Astropart. Phys.* **73**, 44 (2016)
34. V. Verzi for the Pierre Auger Collaboration, in *33th ICRC* (Rio de Janeiro, Brazil), **928**
35. A. Aab, et al., *Phys. Rev. Lett.* **117**, 192001 (2016)
36. L. Cazón for the Pierre Auger Collaboration, in *UHECR Conf.* (Paris, France, 2018), EPJ Web Conf. **210**, 02002
37. The Pierre Auger Collaboration, *Phys. Rev. D* **91**, 032003 (2015)
38. H. Dembinski for the Working Group on Hadronic Interactions and Shower Physics, in *UHECR Conf.* (Paris, France, 2018), EPJ Web Conf. **210**, 02004
39. A. Glushkov et al., *JETP Lett.* **87**, 190 (2008)
40. T. Abu-Zayyad et al., *Phys. Rev. Lett.* **84**, 4276 (2000)
41. J.A. Bellido et al., *Phys. Rev. D* **98**, 023014 (2018)
42. R.U. Abbasi et al., *Phys. Rev. D* **98**, 022002 (2018)
43. The Pierre Auger Collaboration, [arXiv:1604.03637](https://arxiv.org/abs/1604.03637) (2016)

The Pierre Auger Collaboration

A. Aab⁷⁵, P. Abreu⁶⁷, M. Aglietta^{49,50}, J. M. Albury¹², I. Allekotte¹, A. Almela^{8,11}, J. Alvarez Castillo⁶³, J. Alvarez-Muñiz⁷⁴, G. A. Anastasi^{49,58}, L. Anchordoqui⁸², B. Andrada⁸, S. Andringa⁶⁷, C. Aramo⁴⁷, P. R. Araújo Ferreira³⁹, H. Asorey⁸, P. Assis⁶⁷, G. Avila^{9,10}, A. M. Badescu⁷⁰, A. Bakalova³⁰, A. Balaceanu⁶⁸, F. Barbato^{47,56}, R. J. Barreira Luz⁶⁷, K. H. Becker³⁵, J. A. Bellido¹², C. Berat³⁴, M. E. Bertaina^{49,58}, X. Bertou¹, P. L. Biermann^b, T. Bister³⁹, J. Biteau³², A. Blanco⁶⁷, J. Blazek³⁰, C. Bleve³⁴, M. Boháčová³⁰, D. Boncioli^{43,43}, C. Bonifazi²⁴, L. Bonneau Arbeletche¹⁹, N. Borodai⁶⁴, A. M. Botti⁸, J. Brack^e, T. Bretz³⁹, F. L. Briechele³⁹, P. Buchholz⁴¹, A. Bueno⁷³, S. Buitink¹⁴, M. Buscemi^{44,54}, K. S. Caballero-Mora⁶², L. Caccianiga⁵⁵, L. Calcagni⁴, A. Cancio^{8,11}, F. Canfora^{75,77}, I. Caracas³⁵, J. M. Carceller⁷³, R. Caruso^{44,54}, A. Castellina^{49,50}, F. Catalani¹⁷, G. Cataldi⁴⁵, L. Cazon⁶⁷, M. Cerda⁹, J. A. Chinellato²⁰, K. Choi¹³, J. Chudoba³⁰, L. Chytka³¹, R. W. Clay¹², A. C. Cobos Cerutti⁷, R. Colalillo^{47,56}, A. Coleman⁸⁸, M. R. Coluccia^{45,52}, R. Conceição⁶⁷, A. Condorelli^{42,43}, G. Consolati^{46,51}, F. Contreras^{9,10}, F. Convenga^{45,52}, C. E. Covault^{80,h}, S. Dasso^{3,5}, K. Daumiller³⁷, B. R. Dawson¹², J. A. Day¹², R. M. de Almeida²⁶, J. de Jesús^{8,37}, S. J. de Jong^{75,77}, G. De Mauro^{75,77}, J. R. T. de Mello Neto^{24,25}, I. De Mitri^{42,43}, J. de Oliveira²⁶, D. de Oliveira Franco²⁰, V. de Souza¹⁸, J. Debatin³⁶, M. del Río¹⁰, O. Deligny³², N. Dhital⁶⁴, A. Di Matteo⁴⁹, M. L. Díaz Castro²⁰, C. Dobrigkeit²⁰, J. C. D'Olivo⁶³, Q. Dorosti⁴¹, R. C. dos Anjos²³, M. T. Dova⁴, J. Ebr³⁰, R. Engel^{36,37}, I. Epicoco^{45,52}, M. Erdmann³⁹, C. O. Escobar^c, A. Etchegoyen^{8,11}, H. Falcke^{75,77,78}, J. Farmer⁸⁷, G. Farrar⁸⁵, A. C. Fauth²⁰, N. Fazzini^c, F. Feldbusch³⁸, F. Fenu^{49,58}, B. Fick⁸⁴, J. M. Figueira⁸, A. Filipčič^{71,72}, M. M. Freire⁶, T. Fujii^{87,f}, A. Fuster^{8,11}, C. Galea⁷, C. Galelli^{46,55}, B. García⁷, A. L. Garcia Vegas³⁹, H. Gemmeke³⁸, F. Gesualdi^{8,37}, A. Gherghel-Lascu⁶⁸, P. L. Ghia³², U. Giaccari⁷⁵, M. Giammarchi⁴⁶, M. Giller⁶⁵, J. Glombitza³⁹, F. Gobbi⁹, G. Golup¹, M. Gómez Berisso¹, P. F. Gómez Vitale^{9,10}, J. P. Gongora⁹, N. González⁸, I. Goos^{1,37}, D. Góra⁶⁴, A. Gorgi^{49,50}, M. Gottowik³⁵, T. D. Grubb¹², F. Guarino^{47,56}, G. P. Guedes²¹, E. Guido^{49,58}, S. Hahn^{8,37}, R. Halliday⁸⁰, M. R. Hampel⁸, P. Hansen⁴, D. Harari¹, V. M. Harvey¹², A. Haungs³⁷, T. Hebbeker³⁹, D. Heck³⁷, G. C. Hill¹², C. Hojvat^c, J. R. Hörandel^{75,77}, P. Horvath³¹, M. Hrabovsky³¹, T. Huege^{14,37}, J. Hulsman^{8,37}, A. Insolia^{44,54}, P. G. Isar⁶⁹, J. A. Johnsen⁸¹, J. Jurysek³⁰, A. Kääpä³⁵, K. H. Kampert³⁵, B. Keilhauer³⁷, J. Kemp³⁹, H. O. Klages³⁷, M. Kleifges³⁸, J. Kleinfeller⁹, M. Köpke³⁶, G. Kuvec Mezek⁷¹, B. L. Lago¹⁶, D. LaHurd⁸⁰, R. G. Lang¹⁸, M. A. Leigui de Oliveira²², V. Lenok³⁷, A. Letessier-Selvon³³, I. Lhenry-Yvon³², D. Lo Presti^{44,54}, L. Lopes⁶⁷, R. López⁵⁹, A. López Casado⁷⁴, R. Lorek⁸⁰, Q. Luce³⁶, A. Lucero⁸, A. Machado Payeras²⁰, M. Malacari⁸⁷, G. Mancarella^{45,52}, D. Mandat³⁰, B. C. Manning¹², J. Manshanden⁴⁰, P. Mantsch^c, A. G. Mariazzi⁴, I. C. Mariş¹³, G. Marsella^{45,52}, D. Martello^{45,52}, H. Martinez¹⁸, O. Martínez Bravo⁵⁹, M. Mastrodicasa^{43,53}, H. J. Mathes³⁷, J. Matthews⁸³, G. Matthiae^{48,57}, E. Mayotte³⁵, P. O. Mazur^c, G. Medina-Tanco⁶³, D. Melo⁸, A. Menshikov³⁸, K.-D. Merenda⁸¹, S. Michal³¹, M. I. Micheletti⁶, L. Miramonti^{46,55}, D. Mockler¹³, S. Mollerach¹, F. Montanet³⁴, C. Morello^{49,50}, M. Mostafá⁸⁶, A. L. Müller^{8,37}, M. A. Muller^{20,d,24}, S. Müller³⁶, R. Mussa⁴⁹, M. Muzio⁸⁵, W. M. Namasaka³⁵, L. Nellen⁶³, M. Niculescu-Oglinzanu⁶⁸, M. Niechciol⁴¹, D. Nitz^{84,g}, D. Nosek²⁹, V. Novotny²⁹, L. Nožka³¹, A. Nucita^{45,52}, L. A. Núñez²⁸, M. Palatka³⁰, J. Pallotta², M. P. Panetta^{45,52}, P. Papenbreer³⁵, G. Parente⁷⁴, A. Parra⁵⁹, M. Pech³⁰, F. Pedreira⁷⁴, J. Pękala⁶⁴, R. Pelayo⁶¹, J. Peña-Rodríguez²⁸, J. Perez Armand¹⁹, M. Perlin^{8,37}, L. Perrone^{45,52}, C. Peters³⁹, S. Petrera^{42,43}, T. Pierog³⁷, M. Pimenta⁶⁷, V. Pirronello^{44,54}, M. Platino⁸, B. Pont⁷⁵, M. Pothast^{75,77}, P. Privitera⁸⁷, M. Prouza³⁰, A. Puyleart⁸⁴, S. Querschfeld³⁵, J. Rautenberg³⁵, D. Ravignani⁸, M. Reininghaus^{8,37}, J. Ridky³⁰, F. Riehn⁶⁷, M. Risse⁴¹, P. Ristori², V. Rizi^{43,53}, W. Rodrigues de Carvalho¹⁹, J. Rodriguez Rojo⁹, M. J. Roncoroni⁸, M. Roth³⁷, E. Roulet¹, A. C. Rovero⁵, P. Ruehl⁴¹, S. J. Saffi¹², A. Saftoiu⁶⁸, F. Salamida^{43,53}, H. Salazar⁵⁹, G. Salina⁴⁸, J. D. Sanabria Gomez²⁸, F. Sánchez^{8,16}, E. M. Santos¹⁹, E. Santos³⁰, F. Sarazin⁸¹, R. Sarmiento⁶⁷, C. Sarmiento-Cano⁸, R. Sato⁹, P. Savina^{32,45,52}, C. Schäfer³⁷, V. Scherini⁴⁵, H. Schieler³⁷, M. Schimassek^{8,36}, M. Schimp³⁵, F. Schlüter^{8,37}, D. Schmidt³⁶, O. Scholten^{14,76}, P. Schovánek³⁰, F. G. Schröder^{37,88}, S. Schröder³⁵, S. J. Sciutto⁴, M. Scornavacche^{8,37}, R. C. Shellard¹⁵, G. Sigl⁴⁰, G. Silli^{8,37}, O. Sima^{68,h}, R. Šmída⁸⁷, P. Sommers⁸⁶, J. F. Soriano⁸², J. Souchard³⁴, R. Squartini⁹, M. Stadelmaier^{8,37}, D. Stanca⁶⁸, S. Stanič⁷¹, J. Stasielak⁶⁴, P. Stassi³⁴, A. Streich^{8,36}, M. Suárez-Durán²⁸, T. Sudholz¹², T. Suomijärvi³², A. D. Supanitsky⁸, J. Šupík³¹, Z. Szadkowski⁶⁶, A. Taboada³⁶, O. A. Taborda¹, A. Tapia²⁷, C. Timmermans^{75,77}, P. Tobiska³⁰, C. J. Todero Peixoto¹⁷, B. Tomé⁶⁷, G. Torralba Elipse⁷⁴, A. Travaini⁹, P. Travnicek³⁰, C. Trimarelli^{43,53}, M. Trini^{71,h}, M. Tueros⁴, R. Ulrich³⁷, M. Unger³⁷, M. Urban³⁹, L. Vaclavek³¹, J. F. Valdés Galicia⁶³, I. Valiño^{42,43}, L. Valore^{47,56}, A. van Vliet⁷⁵, E. Varela⁵⁹, B. Vargas Cárdenas⁶³, A. Vásquez-Ramírez²⁸, D. Veberič³⁷, C. Ventura²⁵, I. D. Vergara Quispe⁴, V. Verzi⁴⁸, J. Vicha³⁰, L. Villaseñor⁵⁹, J. Vink⁷⁹, S. Vorobiov⁷¹, H. Wahlberg⁴, A. A. Watson^a, M. Weber³⁸, A. Weindl³⁷, L. Wiencke⁸¹, H. Wilczyński⁶⁴, T. Winchen¹⁴, M. Wirtz³⁹, D. Wittkowski³⁵, B. Wundheiler⁸, A. Yushkov³⁰, O. Zapparrata¹³, E. Zas⁷⁴, D. Zavrtanik^{71,72}, M. Zavrtanik^{71,72}, L. Zehrer⁷¹, A. Zepeda⁶⁰, M. Ziolkowski⁴¹, F. Zuccarello^{44,54}

- ¹ Centro Atómico Bariloche and Instituto Balseiro (CNEA-UNCuyo-CONICET), San Carlos de Bariloche, Argentina
- ² Centro de Investigaciones en Láseres y Aplicaciones, CITEDEF and CONICET, Villa Martelli, Argentina
- ³ Departamento de Física and Departamento de Ciencias de la Atmósfera y los Océanos, FCEyN, Universidad de Buenos Aires and CONICET, Buenos Aires, Argentina
- ⁴ IFLP, Universidad Nacional de La Plata and CONICET, La Plata, Argentina
- ⁵ Instituto de Astronomía y Física del Espacio (IAFE CONICET-UBA), Buenos Aires, Argentina
- ⁶ Instituto de Física de Rosario (IFIR) – CONICET/U.N.R. and Facultad de Ciencias Bioquímicas y Farmacéuticas U.N.R., Rosario, Argentina
- ⁷ Instituto de Tecnologías en Detección y Astropartículas (CNEA, CONICET, UNSAM) and Universidad Tecnológica Nacional – Facultad Regional Mendoza (CONICET/CNEA), Mendoza, Argentina
- ⁸ Instituto de Tecnologías en Detección y Astropartículas (CNEA, CONICET UNSAM), Buenos Aires, Argentina
- ⁹ Observatorio Pierre Auger, Malargüe, Argentina
- ¹⁰ Observatorio Pierre Auger and Comisión Nacional de Energía Atómica, Malargüe, Argentina
- ¹¹ Universidad Tecnológica Nacional – Facultad Regional Buenos Aires, Buenos Aires, Argentina
- ¹² University of Adelaide, Adelaide, SA, Australia
- ¹³ Université Libre de Bruxelles (ULB), Brussels, Belgium
- ¹⁴ Vrije Universiteit Brussels, Brussels, Belgium
- ¹⁵ Centro Brasileiro de Pesquisas Físicas, Rio de Janeiro, RJ, Brazil
- ¹⁶ Centro Federal de Educação Tecnológica Celso Suckow da Fonseca, Nova Friburgo, Brazil
- ¹⁷ Universidade de São Paulo, Escola de Engenharia de Lorena, Lorena, SP, Brazil
- ¹⁸ Universidade de São Paulo, Instituto de Física de São Carlos, São Carlos, SP, Brazil
- ¹⁹ Universidade de São Paulo, Instituto de Física, São Paulo, SP, Brazil
- ²⁰ Universidade Estadual de Campinas, IFGW, Campinas, SP, Brazil
- ²¹ Universidade Estadual de Feira de Santana, Feira de Santana, Brazil
- ²² Universidade Federal do ABC, Santo André, SP, Brazil
- ²³ Universidade Federal do Paraná, Setor Palotina, Palotina, Brazil
- ²⁴ Universidade Federal do Rio de Janeiro, Instituto de Física, Rio de Janeiro, RJ, Brazil
- ²⁵ Universidade Federal do Rio de Janeiro (UFRJ), Observatório do Valongo, Rio de Janeiro, RJ, Brazil
- ²⁶ Universidade Federal Fluminense, EEIMVR, Volta Redonda, RJ, Brazil
- ²⁷ Universidad de Medellín, Medellín, Colombia
- ²⁸ Universidad Industrial de Santander, Bucaramanga, Colombia
- ²⁹ Charles University, Faculty of Mathematics and Physics, Institute of Particle and Nuclear Physics, Prague, Czech Republic
- ³⁰ Institute of Physics of the Czech Academy of Sciences, Prague, Czech Republic
- ³¹ Palacky University, RCPTM, Olomouc, Czech Republic
- ³² Université Paris-Saclay, CNRS/IN2P3, IJCLab, Orsay, France
- ³³ Laboratoire de Physique Nucléaire et de Hautes Energies (LPNHE), Universités Paris 6 et Paris 7 CNRS-IN2P3, Paris, France
- ³⁴ Univ. Grenoble Alpes, CNRS, Grenoble Institute of Engineering Univ. Grenoble Alpes, LPSC-IN2P3, 38000 Grenoble, France
- ³⁵ Department of Physics, Bergische Universität Wuppertal, Wuppertal, Germany
- ³⁶ Karlsruhe Institute of Technology, Institute for Experimental Particle Physics (ETP), Karlsruhe, Germany
- ³⁷ Karlsruhe Institute of Technology, Institut für Kernphysik, Karlsruhe, Germany
- ³⁸ Karlsruhe Institute of Technology, Institut für Prozessdatenverarbeitung und Elektronik, Karlsruhe, Germany
- ³⁹ RWTH Aachen University, III. Physikalisches Institut A, Aachen, Germany
- ⁴⁰ Universität Hamburg, II. Institut für Theoretische Physik, Hamburg, Germany
- ⁴¹ Universität Siegen, Fachbereich 7 Physik – Experimentelle Teilchenphysik, Siegen, Germany
- ⁴² Gran Sasso Science Institute, L'Aquila, Italy

- ⁴³ INFN Laboratori Nazionali del Gran Sasso, Assergi, L'Aquila, Italy
- ⁴⁴ INFN, Sezione di Catania, Catania, Italy
- ⁴⁵ INFN, Sezione di Lecce, Lecce, Italy
- ⁴⁶ INFN, Sezione di Milano, Milano, Italy
- ⁴⁷ INFN, Sezione di Napoli, Napoli, Italy
- ⁴⁸ INFN, Sezione di Roma "Tor Vergata", Rome, Italy
- ⁴⁹ INFN, Sezione di Torino, Torino, Italy
- ⁵⁰ Osservatorio Astrofisico di Torino (INAF), Torino, Italy
- ⁵¹ Politecnico di Milano, Dipartimento di Scienze e Tecnologie Aerospaziali, Milano, Italy
- ⁵² Dipartimento di Matematica e Fisica "E. De Giorgi", Università del Salento, Lecce, Italy
- ⁵³ Dipartimento di Scienze Fisiche e Chimiche, Università dell'Aquila, L'Aquila, Italy
- ⁵⁴ Dipartimento di Fisica e Astronomia, Università di Catania, Catania, Italy
- ⁵⁵ Dipartimento di Fisica, Università di Milano, Milano, Italy
- ⁵⁶ Dipartimento di Fisica "Ettore Pancini", Università di Napoli "Federico II", Napoli, Italy
- ⁵⁷ Dipartimento di Fisica, Università di Roma "Tor Vergata", Rome, Italy
- ⁵⁸ Dipartimento di Fisica, Università Torino, Torino, Italy
- ⁵⁹ Benemérita Universidad Autónoma de Puebla, Puebla, Mexico
- ⁶⁰ Centro de Investigación y de Estudios Avanzados del IPN (CINVESTAV), Mexico, D.F., Mexico
- ⁶¹ Unidad Profesional Interdisciplinaria en Ingeniería y Tecnologías Avanzadas del Instituto Politécnico Nacional (UPIITA-IPN), Mexico, D.F., Mexico
- ⁶² Universidad Autónoma de Chiapas, Tuxtla Gutiérrez, Chiapas, Mexico
- ⁶³ Universidad Nacional Autónoma de México, Mexico, D.F., Mexico
- ⁶⁴ Institute of Nuclear Physics PAN, Krakow, Poland
- ⁶⁵ Faculty of Astrophysics, University of Łódź, Łódź, Poland
- ⁶⁶ Faculty of High-Energy Astrophysics, University of Łódź, Łódź, Poland
- ⁶⁷ Laboratório de Instrumentação e Física Experimental de Partículas – LIP and Instituto Superior Técnico – IST, Universidade de Lisboa – UL, Lisbon, Portugal
- ⁶⁸ "Horia Hulubei" National Institute for Physics and Nuclear Engineering, Bucharest-Magurele, Romania
- ⁶⁹ Institute of Space Science, Bucharest-Magurele, Romania
- ⁷⁰ University Politehnica of Bucharest, Bucharest, Romania
- ⁷¹ Center for Astrophysics and Cosmology (CAC), University of Nova Gorica, Nova Gorica, Slovenia
- ⁷² Experimental Particle Physics Department, J. Stefan Institute, Ljubljana, Slovenia
- ⁷³ Universidad de Granada and C.A.F.P.E., Granada, Spain
- ⁷⁴ Instituto Galego de Física de Altas Enerxías (IGFAE), Universidade de Santiago de Compostela, Santiago de Compostela, Spain
- ⁷⁵ IMAPP, Radboud University Nijmegen, Nijmegen, The Netherlands
- ⁷⁶ KVI – Center for Advanced Radiation Technology, University of Groningen, Groningen, The Netherlands
- ⁷⁷ Nationaal Instituut voor Kernfysica en Hoge Energie Fysica (NIKHEF), Science Park, Amsterdam, The Netherlands
- ⁷⁸ Stichting Astronomisch Onderzoek in Nederland (ASTRON), Dwingeloo, The Netherlands
- ⁷⁹ Universiteit van Amsterdam, Faculty of Science, Amsterdam, The Netherlands
- ⁸⁰ Case Western Reserve University, Cleveland, OH, USA
- ⁸¹ Colorado School of Mines, Golden, CO, USA
- ⁸² Department of Physics and Astronomy, Lehman College, City University of New York, Bronx, NY, USA
- ⁸³ Louisiana State University, Baton Rouge, LA, USA
- ⁸⁴ Michigan Technological University, Houghton, MI, USA
- ⁸⁵ New York University, New York, NY, USA
- ⁸⁶ Pennsylvania State University, University Park, PA, USA
- ⁸⁷ University of Chicago, Enrico Fermi Institute, Chicago, IL, USA
- ⁸⁸ University of Delaware, Department of Physics and Astronomy, Bartol Research Institute, Newark, DE, USA

^a School of Physics and Astronomy, University of Leeds, Leeds, United Kingdom

^b Max-Planck-Institut für Radioastronomie, Bonn, Germany

^c Fermi National Accelerator Laboratory, USA

^d also at Universidade Federal de Alfenas, Poços de Caldas, Brazil

^e Colorado State University, Fort Collins, CO, USA

^f now at Hakubi Center for Advanced Research and Graduate School of Science, Kyoto University, Kyoto, Japan

^g also at Karlsruhe Institute of Technology, Karlsruhe, Germany

^h also at Radboud University Nijmegen, Nijmegen, The Netherlands

Reproduced with permission of copyright owner. Further reproduction
prohibited without permission.